Energy &
Environment Nexus

https://doi.org/10.48130/een-0026-0013

Original Research

Open Access

Surface oxygen species dictate reaction pathways in platinum-catalyzed aqueous phase reforming of methanol

Yuyao Yang[1,2#], Xuan Bie[1,2#], Yingbo Zhu[1,2], Xuelong Quan[1,2], Bocheng Yu[1,2], Qinghai Li[1,2], Yanguo Zhang[1,2] and Hui Zhou[1,2*]

Received: 21 March 2026

Revised: 8 May 2026

Accepted: 8 June 2026

Published online: 7 July 2026

Abstract

Aqueous phase reforming of methanol (APRM) enables direct hydrogen release from liquid methanol, offering a safe and efficient approach for hydrogen storage and supply. Pt-based catalysts supported on oxides have been shown to enhance catalytic activity, yet the mechanistic role of surface oxygen species remains poorly understood. Herein, we reveal that oxygen species, including hydroxyls, lattice oxygen, and inert oxygen species, govern the reaction pathways of APRM. Contrary to the common expectation that reactive oxygen species enhance catalytic performance, we uncover that reactive lattice oxygen species limit catalytic activity by over-stabilizing formate intermediates in the water-gas shift reaction (WGS). Instead, amphoteric oxides with hydroxyls (in particular Pt/Al_2O_3) outperform other catalysts, achieving a H_2 production rate of 846.9 μmol g_{Pt}^{-1} s^{-1} and reforming selectivity of 97.3% at 250 °C. This is attributed to the exposed surface hydroxyls, which facilitate the WGS via supplying available OH* reactants and thereby enhance H_2 generation. For inert and weakly reducible oxygen species, the weak metal-support interaction limits the ability of Pt sites to activate methanol toward CO* and H_2 formation. These findings demonstrate that oxygen species dictate reaction pathways and provide mechanistic guidance for designing oxide-supported catalysts for APRM.

Keywords: Aqueous phase reforming of methanol, Oxide species, Platinum-catalyzed, Hydroxyls, Lattice oxygen species, Inert oxygen species

Highlights

- Oxygen species dictate the catalytic performance of aqueous phase reforming of methanol.
- Exposed surface hydroxyls supply available OH^* reactants and enhance H_2 generation to 846.9 μmol g_{Pt}^{-1} s^{-1}.
- Reactive lattice oxygen species promote methanol activation but over-stabilize formate intermediates.
- Inert and weakly reducible oxygen species hinder methanol activation on Pt sites.

# Authors contributed equally: Yuyao Yang and Xuan Bie

* Correspondence: Hui Zhou (huizhou@tsinghua.edu.cn)

Full list of author information is available at the end of the article.

https://doi.org/10.48130/een-0026-0013

Graphical abstract

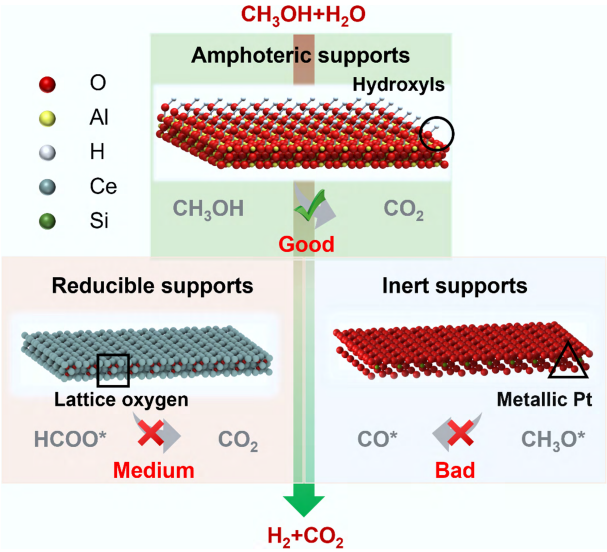

Introduction

The transition to low-carbon energy systems urgently requires near-zero emissions and widely applicable renewable energy sources[1,2], such as hydrogen (H_2)[3,4]. Due to its low volumetric energy density (~3 kW m^{-3})[5,6], H_2 remains challenging to store and transport, restricting its widespread application[7,8]. Methanol stands out owing to its liquid nature under ambient conditions, high H_2 content (12.5 wt%), and ease of conversion[9]. The predominant strategy for H_2 production from methanol is gas-phase steam reforming, in which methanol vapor reacts with steam to generate CO_2 and H_2[10]. However, this process typically requires high operating temperatures (> 300 °C) and an additional vaporization unit[11,12]. Aqueous phase reforming of methanol (APRM, $CH_3OH(l) + H_2O(l) \rightarrow CO_2 + 3H_2$) enables the release of H_2 from the liquid phase at relatively low temperatures (150–250 °C), using compact reactors[13]. Moreover, this method exhibits a low by-product yield, particularly for CO and CH_4, which is advantageous for H_2 utilization in proton exchange membrane fuel cells (PEMFCs). Therefore, APRM is an emerging H_2 release system, particularly attractive for distributed and mobile H_2 supply, such as transportation applications[14].

APRM is limited by unfavorable thermodynamics at low temperatures and high kinetic constraints associated with C–H or O–H bond cleavage in methanol decomposition and water-gas shift[15,16]. Previous studies have shown that Pt nanoparticles supported on oxide supports (e.g., Pt/Al_2O_3, Pt/CeO_2, $Pt/NiAl_2O_4$) are uniquely capable of promoting APRM activity via acid/alkaline sites[17–19], oxygen vacancies[20,21], or metal-support interaction[22–24]. For example, K^+-doped Pt/Al_2O_3 catalysts (PtK_x/Al_2O_3), which possess more alkaline sites, can affect the Pt d-band center and stabilize the *OH intermediates to improve the H_2 production rate[17]. Pt single-atom-loaded oxygen-vacancy-rich CeO_2 catalysts (Pt_1/CeO_2) showed excellent activity in APRM, attributed to the role of Ce^{3+} ions and oxygen vacancies in promoting water activation[20]. $Pt/NiAl_2O_4$ displayed superior activity and stability due to synergistic interaction between Pt and spinel, which facilitated the redox pathway of water-gas shift reaction (WGS, $CO + H_2O \rightarrow CO_2 + H_2$)[22]. Although considerable effort has been devoted to understanding metal active sites and reaction intermediates in APRM, the roles of oxygen species have not been fully understood.

This study elucidates how surface oxygen species, including hydroxyls, lattice oxygen, and inert oxygen species, govern the catalytic performance of APRM. We find that inert oxygen species induce a weak metal-support interaction, and thus the ability of Pt sites to activate methanol toward CO* and H_2 is limited. By contrast, catalysts with surface hydroxyls and reactive oxygen species promote methanol decomposition on Pt sites via strong metal-support interaction and enhance H_2 generation by supplying OH* sources for CO* conversion. Collectively, these findings demonstrate that surface oxygen species dictate catalytic performance and provide mechanistic guidance for the rational design of oxide-supported catalysts for APRM.

Experimental

Catalyst preparation

A series of Pt-based catalysts supported on various oxides (Pt/Al_2O_3, Pt/ZrO_2, Pt/CeO_2, Pt/TiO_2, and Pt/SiO_2) was synthesized via the wet impregnation method. The Pt precursor was $H_2PtCl_6{\cdot}6H_2O$ (8 wt% in water), purchased from Shanghai Macklin Biochemical Co., Ltd. The information on the five supports used is as follows: Al_2O_3 (A766523, Shanghai Macklin Biochemical Co., Ltd), SiO_2 (S861577, Shanghai Macklin Biochemical Co., Ltd), ZrO_2 (J2211262, Shanghai Aladdin Biochemical Technology Co., Ltd), CeO_2 (C103981, Shanghai Aladdin Biochemical Technology Co., Ltd), and TiO_2 (T818930, Shanghai Macklin Biochemical Co., Ltd). Before the impregnation, all oxide supports were calcined at 500 °C for 4 h in air.

For the impregnation process, 1 g of pretreated supports was added to a beaker containing 0.27 g $H_2PtCl_6{\cdot}6H_2O$ solution. Then, 50 mL of deionized water was added to the beaker to obtain a homogeneous suspension. The mixture was continuously stirred at 80 °C overnight until the water had evaporated completely. Finally, the resulting powder was calcined in a muffle or tube furnace at 500 °C for 4 h.

Catalytic performance test

Prior to evaluating catalytic performance, the Pt-based catalysts were reduced in a 10% H_2/N_2 flow at 500 °C for 2 h. After the pretreatment process, 0.1 g of the pre-reduced catalysts and 30 mL of a methanol-water mixture (methanol/water molar ratio of 1:3) were loaded into an autoclave reactor. The sealed autoclave was purged using N_2 to remove the remaining air in the reactor, after which a certain amount of N_2 was introduced as the internal standard. The reactor was subsequently heated from room temperature to the target temperatures (190, 210, 230, or 250 °C) over approximately 30 min, and then maintained at the set temperature for 30 min. After the reaction, the gaseous product (N_2, H_2, CO_2, CO, and CH_4) in the reactor was collected in a gasbag and analyzed by micro gas chromatography (Inficon, Micro GC) using a thermal conductivity detector (TCD). The amount of gas products, including H_2, CO, CO_2, and CH_4, was quantified using the ratio of their peak areas to the internal standard gas (N_2).

To evaluate the catalytic activity, we calculated the average H_2 production rate (R_{H_2}, μmol g_{Pt}^{-1} s^{-1}), which was defined as the amount of H_2 produced per unit mass of Pt per unit time, as shown in Eq. (1). The selectivity of methanol reforming ($S_{reforming}$) and gaseous by-products including CO and CH_4 (S_{CO}, S_{CH_4} %) were calculated by Eqs (2)–(4):

$$R_{H_2} = \frac{n_{H_2}}{t \times m_{Pt}} \quad (1)$$

$$S_{reforming} = \frac{n_{CO_2}}{n_{methanol}} \times 100\% \quad (2)$$

$$S_{CO} = \frac{n_{CO}}{n_{methanol}} \times 100\% \quad (3)$$

$$S_{CH_4} = \frac{n_{CH_4}}{n_{methanol}} \times 100\% \quad (4)$$

In Eqs (1)–(4), m_{Pt} (g) is the amount of Pt loaded on the surface per gram of catalyst (Supplementary Table S1), t (s) is the constant temperature time of the reactor. In the formula for CO, CH_4, and CO_2 selectivity, n_{CO} (μmol), n_{CH_4} (μmol), and n_{CO_2} (μmol) are the mole quantities of CO, CH_4, and CO_2, and $n_{methanol}$ corresponds to the consumed methanol, which is equal to the total molar amount of CO, CO_2, and CH_4.

Catalyst characterization

The morphology of Pt/oxides was investigated by scanning electron microscopy (SEM) and transmission electron microscopy (TEM), using JEOL JEM-2100 Plus and JSM-7900F, respectively. The Pt loading of Pt/oxide catalysts was quantified using inductively coupled plasma–optical emission spectroscopy (ICP-OES, iCAP 7400). Surface areas and pore-size distribution of supports were measured by N_2 isothermal adsorption-desorption (Micromeritics ASAP 2460) using the Brunauer-Emmett-Teller (BET) model. X-ray diffraction (XRD) patterns were collected using a Malvern Panalytical Empyrean diffractometer with Cu Kα radiation over a 2θ range of 10–90° at a step size of 0.0133°. X-ray photoelectron spectroscopy (XPS) was carried out on a Thermo Fisher Scientific ESCALAB 250Xi instrument. The H_2 temperature-programmed reduction (H_2-TPR), CO_2 or NH_3 temperature-programmed desorption (CO_2-TPD, NH_3-TPD) were conducted on Micromeritics AutoChem II 2920. For *in-situ* diffuse reflectance infrared Fourier transform spectroscopy (DRIFTS), measurements were carried out using a Thermo Fisher Nicolet IS50 instrument with a Mercury Cadmium Telluride (MCT) detector. The pretreated catalysts were loaded into the chamber and exposed to N_2, followed by heating to 230 °C. Subsequently, the reactants (CH_3OH/H_2O = 1:3 or pure CH_3OH or H_2O) were introduced to the chamber by N_2 bubbling for 30 min, followed by N_2 purging for another 30 min. Background spectra were collected after the target temperature was reached under an N_2 atmosphere, and then the spectra were collected every 5 min while the reactants were introduced.

Results and discussion

Catalytic performance of APRM

The catalytic activities of various 1 wt% Pt-based catalysts were evaluated across a temperature range of 190–250 °C at different pressures in an autoclave reactor (Supplementary Fig. S1). Regardless of oxide supports, the H_2 production rate increases with increasing temperature (Fig. 1a), which can be attributed to the endothermic nature of APRM[15]. Pt-based catalysts supported on different oxides exhibit markedly different activities. The highest activity is observed for amphoteric oxides (Al_2O_3 and ZrO_2)[25,26], followed by reducible oxides (CeO_2 and TiO_2), and inert SiO_2 displays the lowest activity. At 190 °C, the H_2 production rate over Pt/Al_2O_3 is nearly fourfold higher than that over Pt/CeO_2 and approximately 20 times higher than that over Pt/SiO_2. The activity advantage remained pronounced at 250 °C: Pt/Al_2O_3 exhibited an H_2 production rate of 846.9 μmol g_{Pt}^{-1} s^{-1}, which is nearly 2.5 times higher than Pt/CeO_2 (329.8 μmol g_{Pt}^{-1} s^{-1}), and 20 times higher than Pt/SiO_2 (41.4 μmol g_{Pt}^{-1} s^{-1}) at 250 °C.

The reforming selectivity of Pt/oxide catalysts was evaluated at various temperatures, which shows that except for Pt/ZrO_2, all catalysts exhibit reforming selectivity of around 95% even at 230 °C

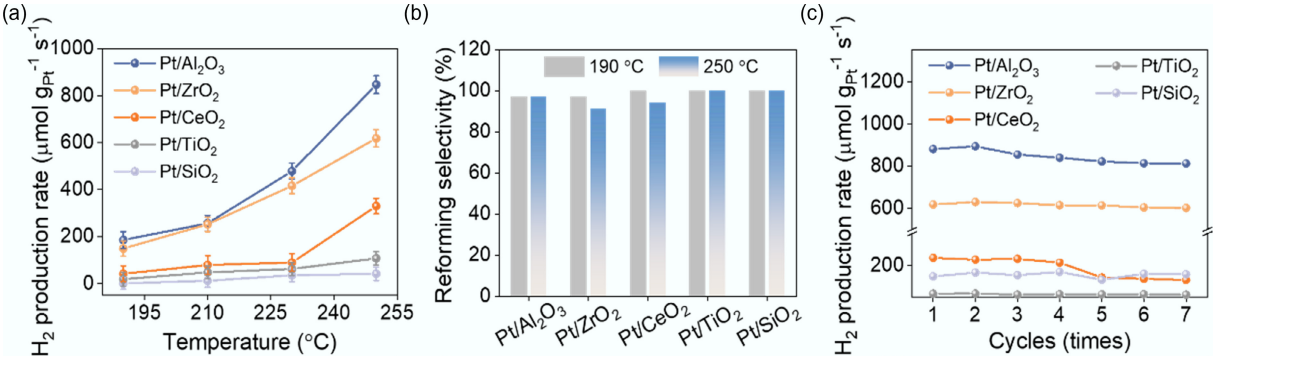

Fig. 1 Catalytic performance of 1 wt% Pt/oxide catalysts. (**a**) H_2 production rates as a function of temperature. (**b**) Reforming selectivity at 190 and 250 °C. (**c**) Stability test over seven cycles at 250 °C. Reaction conditions: 30 mL methanol-water mixture (n[CH_3OH] : n[H_2O] = 1:3), 100 mg catalyst loading, 30 min, 0.5 MPa.

https://doi.org/10.48130/een-0026-0013

(Fig. 1b). Regarding hydrocarbon byproducts, trace amounts of CH_4 can be detected over most Pt/oxide catalysts, while no detectable CH_4 is observed over Pt/TiO_2 and Pt/SiO_2 (Supplementary Figs S2–S6). We propose that the formation of CH_4 occurs under high pressure and H_2-rich atmosphere via CO_2 or CO methanation ($CO_2 + 4H_2 \rightarrow CH_4 + 2H_2O$, $CO + 3H_2 \rightarrow CH_4 + H_2O$)[27]. CO byproducts can poison separation membranes and deactivate PEMFCs[28], making their suppression critically important. Pt/SiO_2 exhibits the lowest CO selectivity, remaining below the detection range of GC from 190 to 250 °C, owing to its limited activity in methanol decomposition (Supplementary Fig. S7). However, as the H_2 production rate increases, the CO selectivity of Pt/Al_2O_3, Pt/CeO_2, Pt/TiO_2, and Pt/ZrO_2 reaches 0.6%, 1.9%, 0.7%, and 4.1%, respectively, at 250 °C. This variation is governed by the two-step mechanism of APRM, which includes methanol decomposition (MD, $CH_3OH \rightarrow CO + 2H_2$) and water-gas shift (WGS, $CO + H_2O \rightarrow CO_2 + H_2$)[21,29]. Higher H_2 production rates typically arise from the concurrent enhancement of MD and the WGS reaction, but an overly accelerated MD pathway may result in elevated CO selectivity[30]. The higher CO selectivity observed over Pt/ZrO_2 originates from a mismatch between the rates of MD and WGS reaction.

Cycling tests were performed to assess the stability of the Pt/oxide catalysts (Fig. 1c). The result shows that most catalysts remain stable over seven cycles with minimal activity loss. Among the tested catalysts, Pt/ZrO_2 shows the highest stability, followed by Pt/SiO_2 and Pt/TiO_2, with only minor activity losses of 2.7%, 6.8%, and 7.3%, respectively. The activity of Pt/CeO_2 decreases sharply after four cycles, from 212.5 to 130.5 μmol g_{Pt}^{-1} s^{-1}, owing to the buildup of the adsorbed intermediates[31]. The most active catalyst, Pt/Al_2O_3, shows a slight deactivation, with activity decreasing from 880.7 to 812.3 μmol g_{Pt}^{-1} s^{-1}. This decline may be attributed to hydroxylation of the oxide support under reaction conditions, possibly leading to aggregation of Pt species[32,33].

Characterization of Pt/oxide catalysts

The different oxide supports all show a spherical morphology, as observed in the SEM images (Supplementary Figs S8–S12) with varying particle sizes. SiO_2 and ZrO_2 particles show the largest particle size (~20 nm), while Al_2O_3, TiO_2, and CeO_2 are significantly smaller (nearly 10 nm). Importantly, after Pt loading, the morphology and particle size of the supports remain largely unchanged (Fig. 2a–e). TEM images further confirm the packed spherical structures of the supports, with Pt nanoparticles uniformly distributed on their surfaces. Statistical analysis reveals that the Pt particles have a narrow size distribution (1.9–3.4 nm) with no evident aggregation. The average Pt particle size increases in the order: Pt/ZrO_2, Pt/CeO_2, Pt/TiO_2, Pt/Al_2O_3, and Pt/SiO_2 (Fig. 2f, Supplementary Figs S13–S17). Notably, Pt/Al_2O_3 shows the highest activity despite having the second-largest Pt particle size, while Pt/ZrO_2 and Pt/CeO_2 with smaller Pt particles exhibit lower activity. No clear correlation is observed between Pt particle size and catalytic activity, suggesting that the dispersion of exposed active sites is not the sole determining factor in catalytic performance.

Multiple characterizations were employed to investigate the physicochemical properties of catalysts, including XRD (Supplementary Fig. S18) and BET (Supplementary Fig. S19, Supplementary Table S2), EPR, XPS, etc. Electron paramagnetic resonance (EPR) spectroscopy was performed to probe unpaired electrons associated with oxygen vacancies. No distinct EPR signal was observed for Pt/Al_2O_3 and Pt/SiO_2, suggesting a negligible concentration of oxygen vacancies (Fig. 3a). In contrast, distinct EPR signals were observed for other Pt/oxide catalysts, indicating the existence of oxygen vacancies. Pt/CeO_2 showed the strongest EPR signal, followed by Pt/ZrO_2, Pt/TiO_2, suggesting a high concentration of oxygen vacancies and active lattice oxygen on Pt/CeO_2, and a similar density of oxygen vacancies on Pt/ZrO_2, Pt/TiO_2.

The O 1s XPS spectra reveal differences in oxygen species among the Pt/oxide catalysts (Fig. 3b). The low binding energy peaks at 529.7–530.8 eV are assigned to lattice oxygen, while the component at 530.8 eV is associated with oxygen vacancies, and the peak at 532.1 eV is attributed to hydroxyl groups[34]. Notably, all catalysts exhibit a lattice oxygen component, while O 1s peaks of Pt/Al_2O_3 and Pt/SiO_2 shift to higher binding energy, suggesting a modification in the local chemical environment of surface oxygen species. Hydroxyls are observed on all catalysts, with the Pt/Al_2O_3 catalyst showing the highest abundance (48.7%), followed by Pt/ZrO_2 (15.6%) (Supplementary Table S3). Oxygen vacancy-related species are detected on Pt/CeO_2, Pt/TiO_2, and Pt/ZrO_2, with abundances decreasing in the order $Pt/CeO_2 > Pt/TiO_2 > Pt/ZrO_2$, consistent with

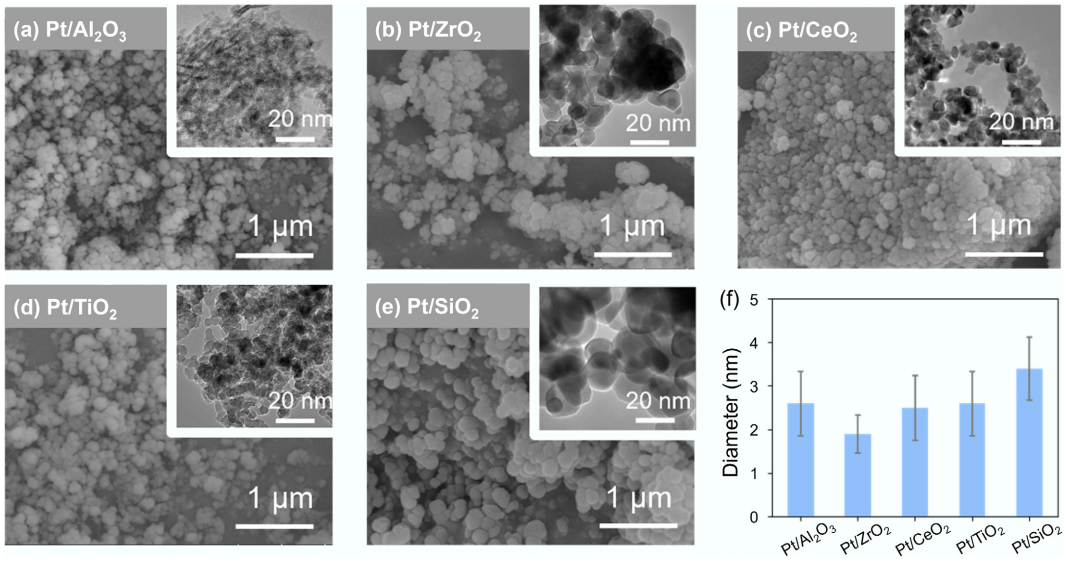

Fig. 2 The morphology characterization of catalysts. (**a**) Pt/Al_2O_3, (**b**) Pt/ZrO_2, (**c**) Pt/CeO_2, (**d**) Pt/TiO_2, (**e**) Pt/SiO_2, and (**f**) Pt particle size distribution.

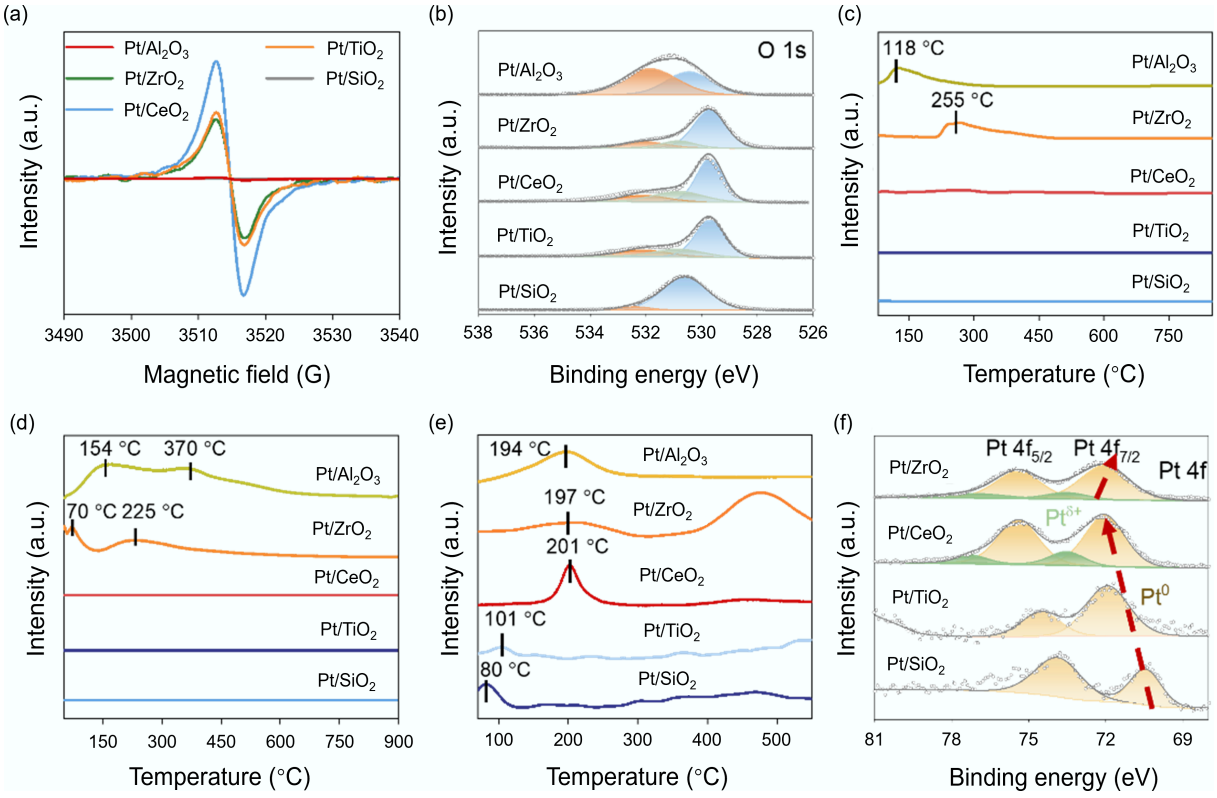

Fig. 3 The structural characterization of Pt/oxide catalysts. (**a**) EPR spectra, (**b**) O 1s XPS, (**c**) NH_3-TPD, (**d**) CO_2-TPD, (**e**) H_2-TPR, and (**f**) Pt 4f XPS.

EPR results. Oxygen vacancies, which can serve as active sites for water dissociation, likely contribute to the improved catalytic activity.

The chemisorption techniques, such as NH_3-TPD, CO_2-TPD, and H_2-TPR experiments, are efficient methods for probing the acid, basic, or reactive properties of catalysts. In the NH_3-TPD profiles (Fig. 3c), obvious desorption peaks appear for Pt/Al_2O_3 and Pt/ZrO_2, while no significant signals are detected for the other catalysts. The peak at 118 °C for Pt/Al_2O_3 corresponds to weak acidic sites, whereas the peak at approximately 255 °C for Pt/ZrO_2 suggests the existence of medium acidic sites[35]. These acidic sites originate from unsaturated surface Al^{3+} and Zr^{4+} species (Lewis acid sites) and surface hydroxyls (Brønsted acid sites). By comparison, the absence of discernible peaks for the other catalysts suggests negligible acidity. Lewis acid sites have been widely associated with enhanced Pt dispersion and redox behavior[32,36], whereas Brønsted acid sites are known to facilitate the water adsorption in APRM.

The CO_2-TPD profiles indicate that both Pt/Al_2O_3 and Pt/ZrO_2 possess a measurable density of basic sites, while the other catalysts show negligible surface basicity (Fig. 3d). The CO_2 desorption peaks for Pt/Al_2O_3 at 154 and 370 °C are assigned to weak and medium basic sites, respectively[37]. In comparison, Pt/ZrO_2 exhibits weaker basicity, with desorption peaks at approximately 70 and 225 °C. It is worth noting that basic sites generally serve as active sites for the WGS reaction by stabilizing OH* intermediates derived from H_2O dissociation[38]. Accordingly, Pt/Al_2O_3 is expected to exhibit a higher WGS capability, which may account for its relatively low CO selectivity.

The redox characteristics of catalysts, which significantly affect the catalytic performance in APRM, were investigated by H_2-TPR and XPS. In the TPR graph, the H_2 consumption peak below 150 °C corresponds to Pt species with weak metal-support interaction. The peak around 200 °C is typically attributed to the reduction of interfacial oxygen species interacting with Pt particles, indicating stronger metal-support interactions[39]. Pt/SiO_2 and Pt/TiO_2 feature the lowest reduction temperature at 80 and 101 °C, proving the existence of weak metal-support interaction (Fig. 3e). This behavior can be ascribed to the chemically inert nature of SiO_2 and the limited redox participation of TiO_2 under mild reduction conditions, which result in minimal electronic coupling between Pt and the supports. The H_2 consumption peaks of Pt/CeO_2, Pt/ZrO_2, and Pt/Al_2O_3 are higher at 201, 197, and 194 °C, owing to the stronger metal-support interaction originating from unsaturated sites. In the case of CeO_2 support, the strong metal-support interaction arises from the oxygen vacancies, whereas in ZrO_2 and Al_2O_3, it is primarily associated with coordinatively unsaturated cationic sites[36].

The high-resolution Pt 4f XPS spectrum exhibits two peaks corresponding to the Pt $4f_{7/2}$ and Pt $4f_{5/2}$ orbitals (Fig. 3f). For Pt/Al_2O_3, the most intense Pt 4f photoemission signal cannot be clearly resolved due to overlap with the strong Al 2p peak[40,41]. Among the other four catalysts, the Pt/SiO_2 shows the lowest binding energy, followed by Pt/TiO_2, indicating a more electron-rich state of Pt species on these supports. The Pt $4f_{7/2}$ spectra of Pt/TiO_2 and Pt/SiO_2 can be deconvoluted into one component at approximately 71.1 and 70.3 eV, which are assigned to metallic Pt^0 species (Supplementary Table S4). In contrast, the Pt 4f peaks of Pt/ZrO_2 and Pt/CeO_2 shift to higher binding energies, as evidenced by the deconvolution of the Pt $4f_{7/2}$ signal into components attributable to Pt^0 and $Pt^{\delta+}$ at approximately 72.8 and 73.6 eV, respectively. This positive binding energy shift suggests electron transfer from Pt nanoparticles to the oxide supports, thereby strengthening the metal-support interaction, consistent with H_2-TPR results. The Pt particles have been regarded as active species for methanol decomposition, especially when strong metal-support interactions are present.

https://doi.org/10.48130/een-0026-0013

Role of oxygen species on APRM

In-situ DRIFTS was employed to monitor the evolution of reaction intermediates and identify the nature of active sites during APRM. The samples pretreated under H_2 atmosphere were first exposed to a mixture of CH_3OH and H_2O vapor at 250 °C for 30 min. As shown in Fig. 4a, two bands at around 2,959 and 2,841 cm^{-1} are detected, which are ascribed to chemisorbed CH_3OH and H_2O at Pt sites, respectively[42,43]. With continued exposure, the signals of intermediates, including methoxy (CH_3O*) at 1,586, 1,033 cm^{-1}, CO* at 2,082 cm^{-1}, and formate (HCOO*) at 1,395 cm^{-1} become more intense[44]. Finally, the peaks corresponding to gaseous final product (CO_2, at 2,362 cm^{-1}) are observed (Fig. 4a). This phenomenon suggests that APRM on Pt/Al_2O_3 proceeded via a pathway involving methanol decomposition to CH_3O* species (first step), followed by the formation of CO* (second step), and the final conversion of CO* to CO_2 and H_2 through WGS (last step)[24]. After purging with N_2, the signals corresponding to various intermediates became weaker, indicating their weak adsorption on the catalyst surface. Similar intermediates were detected for the other catalysts, particularly Pt/ZrO_2, suggesting analogous reaction routes (Fig. 4b). For Pt/CeO_2, abundant CH_3O* and HCOO* intermediates can be observed, and these peaks persist even after N_2 purging, indicating strong adsorption of these intermediates on the catalyst surface (Fig. 4c). This strong adsorption behavior may hinder the subsequent conversion of intermediates, thereby limiting the H_2 production. On the surface of Pt/TiO_2 and Pt/SiO_2, only adsorption features corresponding to CH_3O* signals are observed, whereas no CO* and HCOO* species are detected (Fig. 4d, e). This behavior arises from the weak interaction between the Pt sites and the inert oxygen species, which limits the activity of MD, particularly the further decomposition of CH_3O*.

We also integrated the HCOO* bands to enable a semi-quantitative comparison of both the formation behavior and the relative

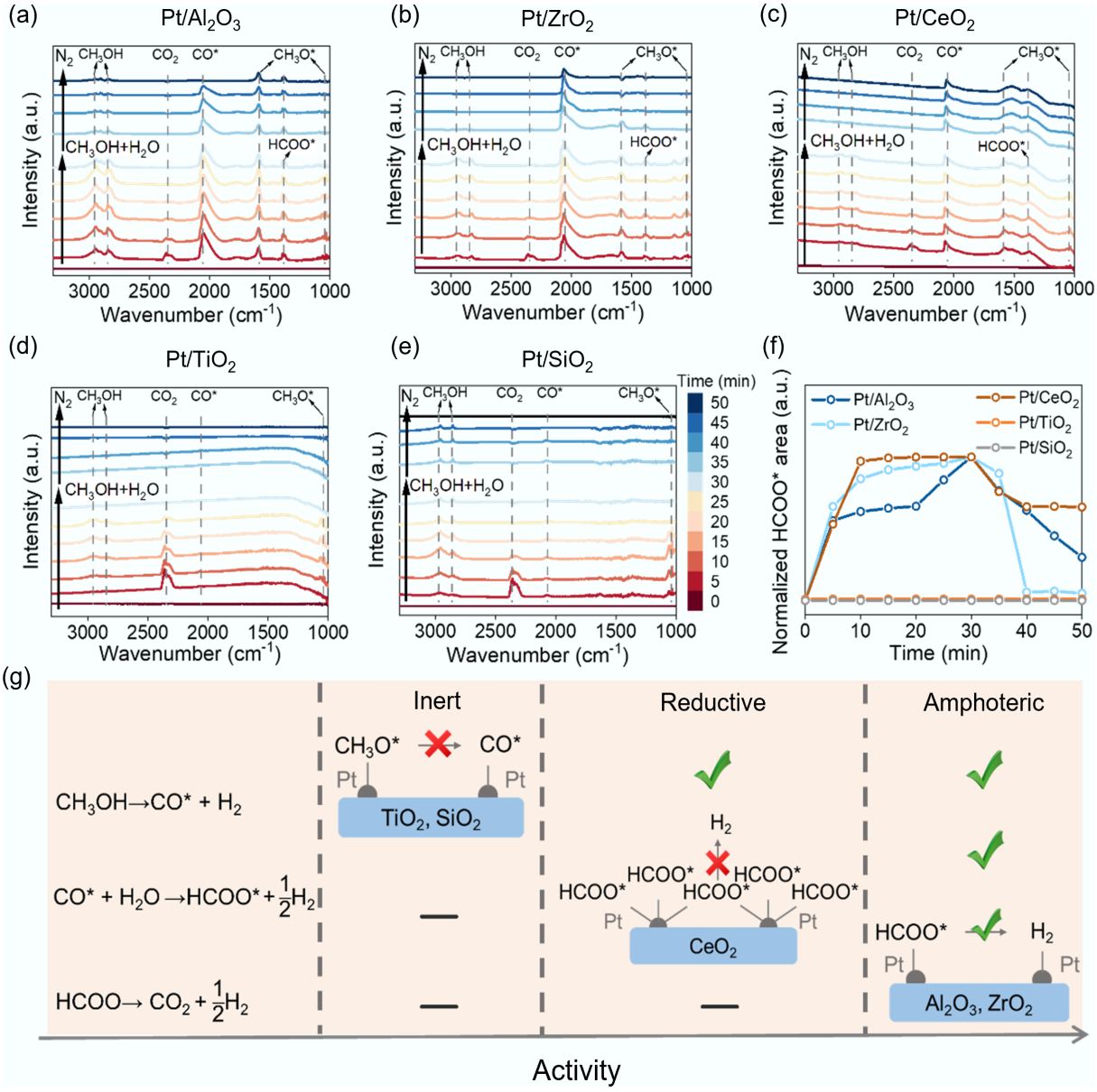

Fig. 4 The catalytic mechanism of Pt/oxide catalysts. The *in-situ* DRIFTS of APRM over (**a**) Pt/Al_2O_3, (**b**) Pt/ZrO_2, (**c**) Pt/CeO_2, (**d**) Pt/TiO_2, and (**e**) Pt/SiO_2 under CH_3OH/H_2O (1:3) at 230 °C. (**f**) The normalized integrated peak area of surface HCOO* (1,395 cm^{-1}). (**g**) Schematic illustration of the APRM reaction pathways over Pt/oxide catalysts.

abundance of HCOO* species over the different catalysts (Fig. 4f). Notably, the peak areas of Pt/TiO_2 and Pt/SiO_2 are barely detectable, indicating that the HCOO* species cannot be formed on their surfaces. In contrast, the normalized HCOO* areas on Pt/Al_2O_3 and Pt/ZrO_2 gradually increase upon methanol introduction, but decrease during N_2 purging, with a small amount of HCOO* remaining on their surfaces. This suggests that HCOO* species are weakly adsorbed on the catalyst surface and are prone to participate in subsequent WGS reactions[43]. On Pt/CeO_2, a large amount of HCOO* signal appears and remains even after N_2 purging. This persistence indicates the formation of strongly adsorbed HCOO* species, which likely block active sites and consequently inhibit the catalytic performance of Pt/CeO_2.

We systematically summarized the mechanism of Pt-based catalysts supported on different types of oxides (Fig. 4g). On weakly reducible and inert oxide supports (TiO_2 and SiO_2), APRM is largely restricted by CO* generation steps (first step), owing to the restriction of MD by weak metal-support interaction induced by inert oxygen species. Over strongly reducible oxides with active oxygen species (e.g., CeO_2), the strongly adsorbed HCOO* intermediates hinder the H_2 production step in WGS (second step), thereby limiting the overall reforming activity. On amphoteric oxides with hydroxyls like Al_2O_3 and ZrO_2, methanol reforming proceeds readily via the MD and WGS pathway (third step), resulting in a relatively high H_2 production rate.

We also carried out the *in-situ* DRIFTS by introducing CH_3OH and H_2O in sequence to probe the role of the catalysts in promoting methanol and water dissociation. On Pt/SiO_2 and Pt/TiO_2, only the limited MD reaction can happen, due to the obvious CH_3O* intermediates at 1,586, 1,033 cm^{-1} and nearly undetectable CO* (2,082 cm^{-1}) in the DRIFTS graph (Fig. 5a, Supplementary Fig. S20). After introducing H_2O, the CH_3O* species are converted into final products (CO_2 and H_2) via WGS[30]. We proposed that poor catalytic performance originated from the weak metal-support interaction

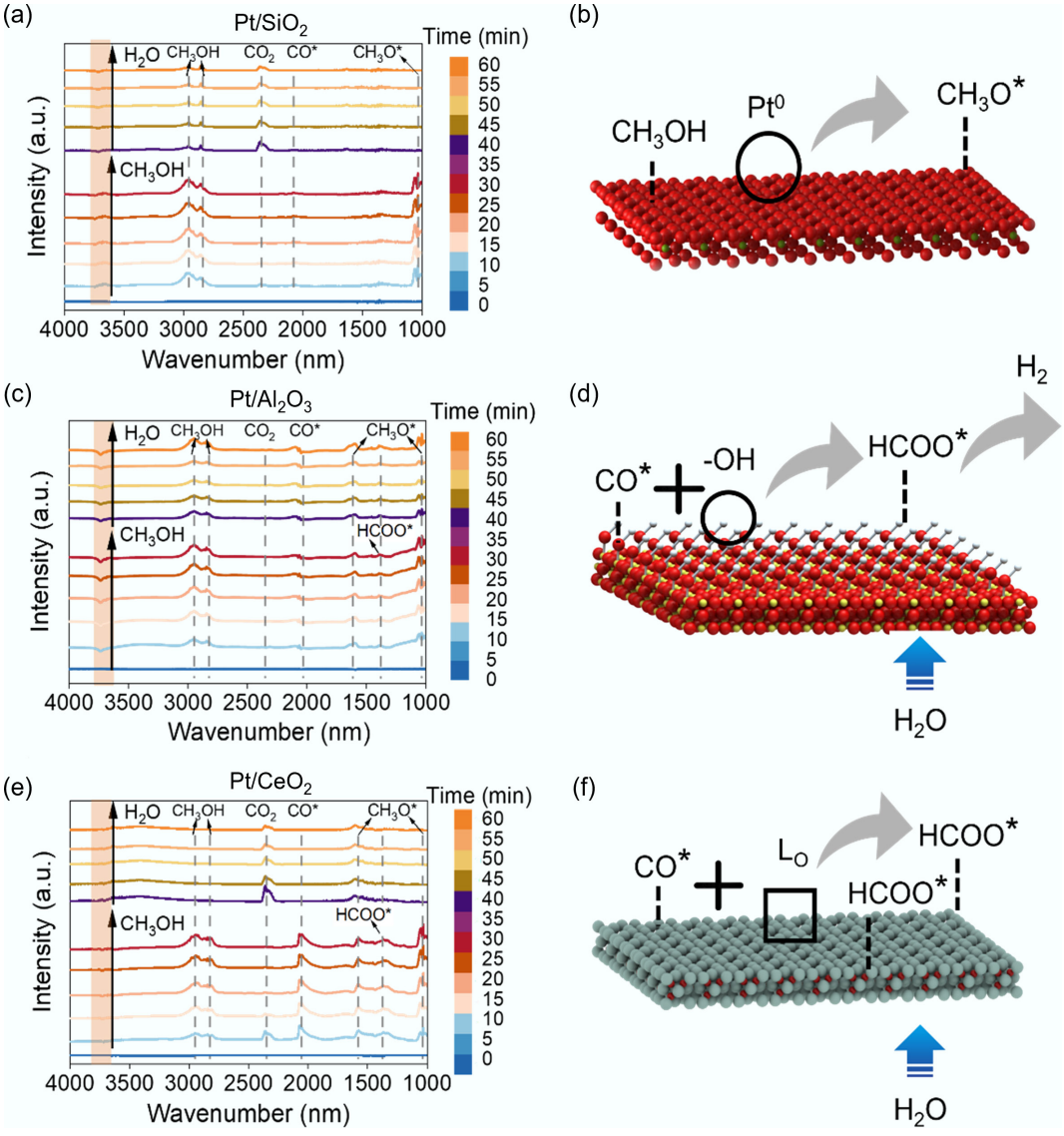

Fig. 5 Effects of surface oxygen species on APRM over Pt/oxide catalysts. (**a**) *In-situ* DRIFTS over Pt/SiO_2 catalyst upon the separate introduction of methanol and water. (**b**) Schematic illustration of the role of inert oxygen species on Pt/SiO_2 in methoxy formation. (**c**) *In-situ* DRIFTS over the Pt/Al_2O_3 catalyst upon separate introduction of methanol and water. (**d**) Schematic illustration of the role of hydroxyls on Pt/Al_2O_3 in formate formation. (**e**) *In-situ* DRIFTS over Pt/CeO_2 catalyst upon separate introduction of methanol and water. (**f**) Schematic illustration of the role of reactive lattice oxygen on Pt/CeO_2 in formate formation.

between Pt and inert oxygen species on inert and weakly reducible oxide-based catalysts. Although they may possess water activation ability, their rate-limiting step is MD to H_2 and CO* (Fig. 5b).

On Pt/Al_2O_3 and Pt/ZrO_2, the decomposition of CH_3OH over Pt/Al_2O_3 occurred, producing abundant intermediates including CH_3O* and CO* (Fig. 5c, Supplementary Fig. S21). It is worth noting that the HCOO* species (requiring an additional oxygen source) formed on Pt/Al_2O_3 via the consumption of surface hydroxyls, as evidenced by the decrease of the surface hydroxyls at ~3,700 cm^{-1}[38,45]. After introducing H_2O, the intensity of OH groups improved, and the previously formed CO* species rapidly disappeared, which can be attributed to the rapid H_2O activation and the occurrence of WGS. Therefore, we proposed that both CH_3OH and H_2O activation proceed rapidly on Pt/Al_2O_3. MD occurred efficiently on Pt sites, while surface OH acted as OH* intermediates to facilitate the conversion of CO*, thereby accelerating the H_2 production rate (Fig. 5d). Meanwhile, these surface OH can be continuously replenished through water dissociation, sustaining the reaction cycle. We also carried out the *in-situ* DRIFTS over Pt/nanorod Al_2O_3 and Pt/nanosheet Al_2O_3 to explore the applicability. Pt/Al_2O_3 with various morphologies proceeds via a hydroxyl-mediated route, as proved by the decrease of the ~3,700 cm^{-1} band assigned to hydroxyls (Supplementary Figs S22 and S23). These results indicate that morphology is not the dominant factor and that surface oxygen species play a more critical role.

As for Pt/CeO_2, the decomposition of CH_3OH proceeded effectively, as evidenced by the appearance of CH_3O* and CO* (Fig. 5e). Subsequently, HCOO* species, which typically require an additional oxygen source, were formed without noticeable changes in the intermediate signals. Compared with Pt/Al_2O_3, HCOO* intermediates were not formed via consumption of surface hydroxyls, but are instead associated with reactive lattice oxygen. We propose that HCOO* formation on Pt/CeO_2 proceeds via a redox pathway involving the consumption of lattice oxygen[46,47]. The introduction of H_2O led to the consumption of CO* intermediates and the formation of gaseous CO_2, indicating Pt/CeO_2 possessed a strong capability for WGS. However, CH_3O* and HCOO* intermediates still can be observed on Pt/CeO_2. This indicates that these species are strongly adsorbed on the catalyst surface, hindering the production of H_2. Therefore, we propose that Pt particle sites serve as active sites for MD, while the active lattice oxygen species provide OH* for CO* conversion (Fig. 5f). However, the adsorption strength of the key intermediate of WGS (HCOO*) is so strong that it limits the H_2 generation. This phenomenon is also observed on other CeO_2-based catalysts like Pt/nanorod CeO_2, where strongly adsorbed HCOO* intermediates form via consumption of lattice oxygen (Supplementary Fig. S24). It can be evidenced by the high intensity signal of HCOO* at 1,395 cm^{-1} and the negligible change in the 3,700 cm^{-1} band.

Conclusion

In this study, we reveal that oxygen species, including hydroxyls, active lattice oxygen, and inert oxygen species, govern the catalytic performance of APRM by modulating methanol activation and the evolution pathways of HCOO*. Amphoteric oxides with hydroxyls outperform other catalysts owing to the oxygen supply effects of exposed surface hydroxyls. In contrast, inert and overly reactive oxygen species lead to limited activity due to weak metal-support interactions or over-stabilization of HCOO* intermediates. These findings establish surface oxygen species as a key descriptor for APRM catalytic performance and provide mechanistic guidance for the rational design of oxide-supported catalysts. The key novelty of this work is the mechanistic classification and specific roles of oxygen species in APRM, rather than the identification of an isolated pathway for a single catalyst.

Supplementary information

It accompanies this paper at: https://doi.org/10.48130/een-0026-0013.

Author contributions

The authors confirm contribution to the paper as follows: Yuyao Yang, Xuan Bie: study conception and design; Yuyao Yang: data collection; Yingbo Zhu, Xuelong Quan: analysis and interpretation of results; Bocheng Yu: data curation; Yuyao Yang: draft manuscript preparation; Qinghai Li: result validation; Yanguo Zhang: project administration; Hui Zhou: supervision. All authors reviewed the results and approved the final version of the manuscript.

Data availability

The data that support the findings of this study are available from the corresponding author upon reasonable request.

Funding

This work was supported by the Beijing Natural Science Foundation (Grant No. JQ24053), the S & T Program of Hebei (Grant No. 254X9917D), International Joint Mission on Climate Change and Carbon Neutrality, Natural Science Foundation of Shanxi Province (Grant Nos 202403021211024, 202403021212148), Tsinghua University Initiative Scientific Research Program, Tsinghua-Jiangyin Innovation Special Fund (Grant Nos TJISF, 2025JYTH0205), and Creative Seed Fund of Shanxi Research Institute for Clean Energy, Tsinghua University.

Declarations

Competing interests

The authors declare that they have no conflict of interest.

Author details

[1]Key Laboratory for Thermal Science and Power Engineering of Ministry of Education, Beijing Key Laboratory of CO_2 Utilization and Reduction Technology, Department of Energy and Power Engineering, Tsinghua University, Beijing 100084, China; [2]Shanxi Research Institute for Clean Energy, Tsinghua University, Taiyuan, Shanxi 030000, China

References

[1] Wei J, Bai Q, Li C, Chen D, Sun Z, et al. 2026. *In situ* generation of high-loading asymmetric metal cluster catalysts via 2D confinement for enhanced electrocatalysis. *Advanced Functional Materials* 36:e25281

[2] Huangfu J, Feng P, Di X, Tian Y, Shi M, et al. 2025. Controllable construction of active sites for catalytic conversion and spatial constraints applied to high-performance lithium–sulfur batteries. *Advanced Energy Materials* 15:2502210

[3] Naseem K, Qin F, Khalid F, Suo G, Zahra T, et al. 2025. Essential parts of hydrogen economy: hydrogen production, storage, transportation and application. *Renewable and Sustainable Energy Reviews* 210:115196

[4] Yan J. 2018. Negative-emissions hydrogen energy. *Nature Climate Change* 8:560–561

[5] Lubitz W, Tumas W. 2007. Hydrogen: an overview. *Chemical Reviews* 107:3900–3903

[6] Meca VL, d'Amore-Domenech R, Crucelaegui A, Leo TJ. 2022. Large-scale maritime transport of hydrogen: economic comparison of liquid

hydrogen and methanol. *ACS Sustainable Chemistry & Engineering* 10:4300–4311

[7] Graetz J. 2009. New approaches to hydrogen storage. *Chemical Society Reviews* 38:73–82

[8] Usman MR. 2022. Hydrogen storage methods: review and current status. *Renewable and Sustainable Energy Reviews* 167:112743

[9] Simon Araya S, Liso V, Cui X, Li N, Zhu J, et al. 2020. A review of the methanol economy: the fuel cell route. *Energies* 13:596

[10] Guo C, Li M, Guo W, Xie J, Qin H, et al. 2024. Quench-induced Cu-ZnO catalyst for hydrogen production from methanol steam reforming. *Chemical Engineering Journal* 486:150331

[11] Köwitsch N, Thoni L, Klemmed B, Benad A, Paciok P, et al. 2021. Proving a paradigm in methanol steam reforming: catalytically highly selective In_xPd_y/In_2O_3 interfaces. *ACS Catalysis* 11:304–312

[12] Ranjekar AM, Yadav GD. 2021. Steam reforming of methanol for hydrogen production: a critical analysis of catalysis, processes, and scope. *Industrial & Engineering Chemistry Research* 60:89–113

[13] Cortright RD, Davda RR, Dumesic JA. 2002. Hydrogen from catalytic reforming of biomass-derived hydrocarbons in liquid water. *Nature* 418:964–967

[14] Lin L, Zhou W, Gao R, Yao S, Zhang X, et al. 2017. Low-temperature hydrogen production from water and methanol using Pt/α-MoC catalysts. *Nature* 544:80–83

[15] Pipitone G, Zoppi G, Pirone R, Bensaid S. 2022. A critical review on catalyst design for aqueous phase reforming. *International Journal of Hydrogen Energy* 47:151–180

[16] Meng H, Yuan S, Yin Z, Shen T, Feng K, et al. 2026. Lattice hydroxyl-assisted platinum single atom catalyst toward hydrogen production from methanol aqueous reforming. *Angewandte Chemie International Edition* 138:e4185228

[17] Wang Y, Liu B, Guo Q, Sun Y, Zhang S, et al. 2023. Stabilized *OH species by K^+-doped Pt for H_2 generation with ultra-low levels of CO through aqueous-phase reforming of methanol at low temperature. *Applied Catalysis B: Environment and Energy* 338:123011

[18] Goma D, Delgado JJ, Lefferts L, Faria J, Calvino JJ, et al. 2019. Catalytic performance of Ni/CeO_2/X-ZrO_2 (X = Ca, Y) catalysts in the aqueous-phase reforming of methanol. *Nanomaterials* 9:1582

[19] Tang Z, Monroe J, Dong J, Nenoff T, Weinkauf D. 2009. Platinum-loaded NaY zeolite for aqueous-phase reforming of methanol and ethanol to hydrogen. *Industrial & Engineering Chemistry Research* 48:2728–2733

[20] Zhang S, Liu Y, Zhang M, Ma Y, Hu J, et al. 2022. Sustainable production of hydrogen with high purity from methanol and water at low temperatures. *Nature Communications* 13:5527

[21] Yu S, Sun Z, Sun Z. 2025. Anchoring $Cu^{\delta+}$ at oxygen-vacancy-rich Y-O_v-Cr interfaces: a self-activated catalyst for ultra-stable and highly selective methanol reforming. *Applied Catalysis B: Environment and Energy* 378:125648

[22] Li D, Li Y, Liu X, Guo Y, Pao CW, et al. 2019. $NiAl_2O_4$ spinel supported Pt catalyst: high performance and origin in aqueous-phase reforming of methanol. *ACS Catalysis* 9:9671–9682

[23] Tian Z, Zhang W, Liu T, Liu J, Wang C, et al. 2022. Study on the promotion of FeO_x species on water-gas shift reaction in methanol aqueous phase reforming over PtFe/Al_2O_3 catalyst. *International Journal of Hydrogen Energy* 47:41468–41479

[24] Wang X, Li D, Gao Z, Guo Y, Zhang H, et al. 2023. The nature of interfacial catalysis over Pt/$NiAl_2O_4$ for hydrogen production from methanol reforming reaction. *Journal of the American Chemical Society* 145:905–918

[25] Barreau M, Courtois X, Can F. 2018. FT-IR spectroscopy study of HNCO adsorption and hydrolysis over oxide-based samples dedicated to deNO_x processes. *Applied Catalysis A: General* 552:147–153

[26] Promhuad P, Sawatmongkhon B, Theinnoi K, Wongchang T, Chollacoop N, et al. 2024. Effect of metal oxides (CeO_2, ZnO, TiO_2, and Al_2O_3) as the support for silver-supported catalysts on the catalytic oxidation of diesel particulate matter. *ACS Omega* 9:19282–19294

[27] Liao Y, Wu D, Rezayan A, Zhao J, Xu C. 2025. Advances in catalysts for production of renewable H_2/CH_4 by aqueous phase reforming (APR) of biomass-derived oxygenates. *Applications in Energy and Combustion Science* 24:100415

[28] Zhang J, Zhao J, Jin C, Chen Z, Liu J. 2022. Self-strained platinum clusters with finite size: high-performance catalysts with CO tolerance for PEMFCs. *ACS Applied Materials & Interfaces* 14:30692–30703

[29] Zhang M, Liu Z, Yan Y, Liu D, Xu G, et al. 2025. Optimizing selectivity via steering dominant reaction mechanisms in steam reforming of methanol for hydrogen production. *Nature Communications* 16:1943

[30] Jiang L, Yuan S, Ma J, Deng S, Fang X, et al. 2025. Enhancing the reactivity of Cu/Al_2O_3 for methanol steam reforming through adding CrO_x: unraveling reaction pathways and the mechanism for improvement. *ACS Catalysis* 15:7138–7152

[31] Liu X, Ruettinger W, Xu X, Farrauto R. 2005. Deactivation of Pt/CeO_2 water-gas shift catalysts due to shutdown/startup modes for fuel cell applications. *Applied Catalysis B: Environment and Energy* 56:69–75

[32] Yang Y, Bie X, Qi X, Xu Y, Li Q, et al. 2025. Modulating Pt states through hydroxyl control for low-temperature aqueous phase reforming of methanol. *ACS Catalysis* 7:5847–5857

[33] Van Cleve T, Underhill D, Veiga Rodrigues M, Sievers C, Medlin JW. 2018. Enhanced hydrothermal stability of γ-Al_2O_3 catalyst supports with alkyl phosphonate coatings. *Langmuir* 34:3619–3625

[34] Li X, Feng Z, Lu H, Hong X, Li G, et al. 2025. Hydroxyl-oxygen vacancy synergy over In_2O_3–ZrO_2 catalysts: mechanistic insights into CO_2 hydrogenation to methanol. *Journal of Materials Chemistry A* 13:20542–20551

[35] Wang Y, Shi T, Fan QY, Liu Y, Zhang A, et al. 2022. Discovering surface structure and the mechanism of graphene oxide-triggered CeO_2–WO_3/TiO_2 catalysts for NO abatement with NH_3. *ACS Catalysis* 12:8386–8403

[36] Kwak JH, Hu J, Mei D, Yi CW, Kim DH, et al. 2009. Coordinatively unsaturated Al^{3+} centers as binding sites for active catalyst phases of platinum on γ-Al_2O_3. *Science* 325:1670–1673

[37] Vance BC, Najmi S, Kots PA, Wang C, Jeon S, et al. 2023. Structure–property relationships for nickel aluminate catalysts in polyethylene hydrogenolysis with low methane selectivity. *JACS Au* 3:2156–2165

[38] Zhai Y, Pierre D, Si R, Deng W, Ferrin P, et al. 2010. Alkali-stabilized Pt-OH_x species catalyze low-temperature water-gas shift reactions. *Science* 329:1633–1636

[39] Lashina EA, Slavinskaya EM, Stonkus OA, Boronin AI. 2024. Abnormally narrow peaks in TPR-H_2 over Pt/CeO_2: experiment and mathematical modelling. *International Journal of Hydrogen Energy* 89:590–604

[40] Serrano-Ruiz JC, Huber GW, Sánchez-Castillo MA, Dumesic JA, Rodríguez-Reinoso F, et al. 2006. Effect of Sn addition to Pt/CeO_2–Al_2O_3 and Pt/Al_2O_3 catalysts: an XPS, ^{119}Sn Mössbauer and microcalorimetry study. *Journal of Catalysis* 241:378–388

[41] Wang YF, Zhang SL, Deng YX, Luan SH, Wang CK, et al. 2025. PtPdAg nanotrees with low pt content for high CO tolerance within formic acid and methanol electrooxidation. *Rare Metals* 44:300–310

[42] Li D, Xu F, Tang X, Dai S, Pu T, et al. 2022. Induced activation of the commercial Cu/ZnO/Al_2O_3 catalyst for the steam reforming of methanol. *Nature Catalysis* 5:99–108

[43] Lu M, Zheng Z, Lu W, Zhu H, Liao J, et al. 2024. Stable Cu/Cu_2O/CuN_3@NC catalysts for aqueous phase reforming of methanol. *ACS Nano* 18:25636–25646

[44] He S, Zhao M, Zhao P, Ma J, Liu C, et al. 2025. Optimizing electrochemical microenvironment of Ni sites by constructing Ni–WO_2 heterostructure for promoting electrocatalytic conversion of methanol to formate via direct electrooxidation path. *Rare Metals* 44:8593–8608

[45] Fan Y, Wang F, Li R, Liu C, Fu Q. 2023. Surface hydroxyl-determined migration and anchoring of silver on alumina in oxidative redispersion. *ACS Catalysis* 13:2277–2285

[46] Hu W, Tan M, Sundermann A, Low KB, Han N, et al. 2025. Enhanced Pt-TWC catalysis via synergistic Fe-Ce effects and improved redox functionality. *Applied Catalysis B: Environment and Energy* 378:125589

[47] Vignatti C, Avila MS, Apesteguía CR, Garetto TF. 2010. Catalytic and DRIFTS study of the WGS reaction on Pt-based catalysts. *International Journal of Hydrogen Energy* 35:7302–7312